Development and characterisation of bilayered periosteum-inspired composite membranes based on sodium alginate-hydroxyapatite nanoparticles

Noelia L. D'Elía [a], Ramon Rial Silva [b], Javier Sartuqui [a], Daniel Ercoli [c], Juan Ruso [b], Paula Messina [a], Gemma Mestres [d,*]

[a] Department of Chemistry, Universidad Nacional del Sur, INQUISUR-CONICET, B8000CPB Bahía Blanca, Argentina
[b] Soft Matter and Molecular Biophysics Group, Department of Applied Physics, University of Santiago de Compostela, 15782 Santiago de Compostela, Spain
[c] Planta Piloto de Ingeniería Química – PLAPIQUI (UNS-CONICET), Camino La Carrindanga Km 7, 8000 Bahía Blanca, Argentina
[d] Materials Science and Engineering, Science for Life Laboratory, Box 534, 751 21 Uppsala University, Uppsala, Sweden

GRAPHICAL ABSTRACT
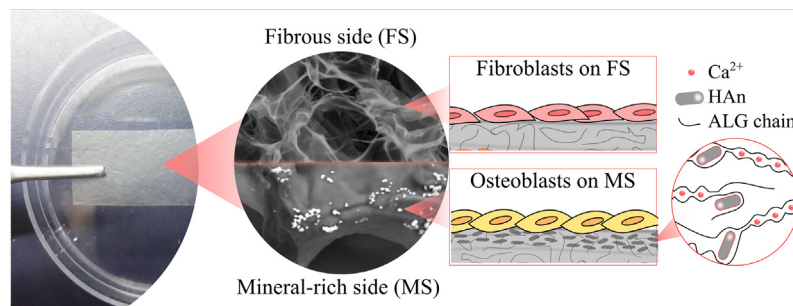
ARTICLE INFO

ABSTRACT

Background and aim: Membranes for guided bone regeneration should have a mechanical structure and a chemical composition suitable for mimicking biological structures. In this work, we pursue the development of periosteum-inspired bilayered membranes obtained by crosslinking alginate with different amounts of nanohydroxyapatite.

Experiments: Alginate-nanohydroxyapatite interaction was studied by rheology and infrared spectroscopy measurements. The membranes were characterized regarding their tensile strength, degradation and surface morphology. Finally, cell cultures were performed on each side of the membranes.

Findings: The ionic bonding between alginate polysaccharide networks and nanohydroxyapatite was proven, and had a clear effect in the strength and microstructure of the hydrogels. Distinct surface characteristics were achieved on each side of the membranes, resulting in a highly porous fibrous side and a mineral-rich side with higher roughness and lower porosity. Moreover, the effect of amount of

Nanohydroxyapatite
Osteoblasts
Periosteum
Rheology

nanohydroxyapatite was reflected in a decrease of the membranes' plasticity and an increment of degradation rate. Finally, it was proved that osteoblast-like cells proliferated and differentiated on the mineral-rich side, specially when a higher amount of nanohydroxyapatite was used, whereas fibroblasts-like cells were able to proliferate on the fibrous side. These periosteum-inspired membranes are promising biomaterials for guided tissue regeneration applications.

1. Introduction

The periosteum is an asymmetric membrane covering most bones in our body. Specifically, it is a dense irregular connective tissue structure, with an outer layer containing fibroblasts and microvessels, and an inner layer containing mostly osteoprogenitor cells [1]. Since the periosteum plays an important role in the remodelling and metabolism of the bone tissue [2], designing new biomaterials that mimic its structure is an appealing strategy for regeneration applications.

Guided bone regeneration (GBR) is a surgical procedure, widely applied in the oral-maxillofacial region, using a barrier membrane to direct the growth of bone while physically preventing the migration of non-osteogenic cells [3]. The significance of this membrane is that it prevents the colonization of the defect by rapidly proliferating epithelium and soft connective tissue, giving instead higher chances to slower-growing cells capable of regenerating bone [3]. In addition, it supports new connective tissue development. Optimally, these biocompatible membranes should be designed with a good flexibility for handling during surgery, an appropriate adhesion to the implanted-site, an adequate strength to provide a good barrier performance, and a biodegradability rate similar to the one of bone formation in the implanted site [3].

An additional challenge is faced as GBR membranes are aimed not only to act as passive barriers but also as promoters of both the bone forming process and wound healing [4]. Being inspired in the periosteum, an active bilayered membrane able to fulfil distinct biological functions on each side could be envisioned. Specifically, the outer side would aim not only to limit the unwanted soft connective tissue growth into the defect but also to support angiogenesis and wound stabilization, while the inner side would protect the underlying blood clot and promote bone tissue regeneration [5].

Although such an asymmetric structure is still underdeveloped in actual commercial formulations [6], new approaches to obtain periosteum-like substitutes are emerging using synthetic polymers. Specially, polycaprolactone-based bilayered membranes have been obtained [1,7,8]; some of them in combination with bioactive nanoparticles such as calcium phosphates [8,9] and Bioglass [6]. However, most of the synthetic polymers have a low wettability and lack of biocompatibility, resulting in moderate nutrients transport through the biomaterial and insufficient cell adhesion on the pore wall [10].

The combination of hydroxyapatite-alginate materials were developed for the first time in the late 1990s for tissue regeneration applications [11]. It was however not until mid 2000 when membranes were made with these materials [12]. Recently, one of our research groups has conceived a bioactive alginate (ALG) composite crosslinked by nanoparticles of hydroxyapatite (HAn) [13]. A beneficial aspect of the aforementioned ALG-HAn hydrogels is their pH-dependent strength properties, as the hydrogel is firm right after implantation due to the acidic environment in healing wounds [14] but degrades along with the tissue healing process. Its biodegradability is important for GBR membranes since a second surgical extraction procedure is avoided [15]. Regarding each compound, ALG is a widely used bioadhesive polymer with potential applications in biomedical science. On the other hand, HAn have been proven to stimulate mesenchymal stem cells adhesion [16], osteoblast differentiation [17,18] and blood clotting [19].

The overall goal of this work was to take a step forward and develop a biodegradable bilayered membrane that rather than merely acting as a passive barrier, would guide bone regeneration on the side facing the bone defect due to its osteoconductive and osteoinductive properties, and would promote wound healing on the other side. For this application, these composites should have appropriate mechanical properties and enhanced biological behaviour. For this purpose, periosteum-inspired bilayered ALG-HAn membranes with different amounts of HAn were synthesised. The interaction between ALG and HAn was evaluated by Fourier transform infrared spectroscopy. Rheological properties of the hydrogels as well as mechanical performance, surface properties and degradation of the final membranes were studied. Finally, osteoblast proliferation and differentiation were tested on the mineral-rich side while fibroblast proliferation on the fibrous side.

2. Experimental section

2.1. Preparation of alginate - nanohydroxyapatite bilayered membranes

Crystalline hydroxyapatite-nanoparticles (HAn), measuring 8 ± 1 nm diameter and 28 ± 3 nm length, were obtained as previously described [17] (**SM**-Figs. 1 and 2). Briefly, an organized network of hexadecyltrimethylammonium bromide (CTAB, 99%, Sigma-Aldrich, ref. n. H5882) micelles in poly(ethylene glycol) 400 (PEG 400, Sigma-Aldrich, ref. n. 202398) were used as template of the nanoparticles. Inorganic precursors, $CaCl_2$ (99%, Sigma-Aldrich, ref. n. C1016), Na_3PO_4 (96%, Sigma-Aldrich, ref. n. 342483) and $NaNO_2$ (97%, Sigma-Aldrich, ref. n. 237213) were sequentially added to the CTAB-PEG solution, followed by a hydrothermal treatment. The final product was filtrated with filter paper (pore size 2.5 μm, Whatman® Grade 42) and calcined at 400 °C for 3 h.

ALG-HAn bilayered membranes were synthesized using a modified version of Benedini et al. synthesis [13]. A 2% w/v solution of alginic acid (from brown algae, ref. n. A7003, Sigma-Aldrich) in water was kept under stirring at 350 rpm for 3 h at 40 °C. Afterwards, 4.5 mL aliquots of the ALG solution were added to 35 mm diameter Petri dishes and left drying at 45 °C for 24 h. Meanwhile, three different fresh crosslinking solutions containing a constant concentration of $CaCl_2$ (110 mM) and increasing concentrations of HAn (0.11, 0.55 and 1.1% w/v in water) were prepared. The crosslinking solutions were sonicated for 1 h and added into empty 35 mm Petri dishes. Subsequently, ALG films were carefully placed on top of the solution to avoid wrinkles and bubbles formation. Finally, hydrogels were stirred on an orbital shaker at 150 rpm, at room temperature for 3 h, to ensure a complete crosslinking and drying. The three membranes synthesized were named in accordance with the content of HAn, herein M-0.11, M-0.55 and M-1.1, respectively. Membranes without HAn served as controls

and were named M-0. Membranes thicknesses used for all the experiments were measured using a compact length measuring instrument (Millimar C1208 PE) (Table S.M. 3).

2.2. Rheological characterisation of the hydrogels

A rheological study was performed to test the influence of HAn concentration on the mechanical properties of fresh hydrogels. For this study, a stress-controlled rheometer (Anton Paar MCR 302) with a parallel plate of 25 mm diameter was used. A Peltier cell and a humidity chamber were used to control the temperature and humidity. The gap was maintained constant to 1 mm through all the experiments.

The hydrogels were synthesized as explained before (last drying step was skipped) and transferred fresh in the rheometer. The hydrogels were maintained with no movement in the rheometer's humidity chamber for 15 min to reach equilibrium before proceeding with the measurements to minimize differences in temperature and uniformity.

To assure an accurate evaluation of the relationships between molecular structure and viscoelastic behaviour experiments were conducted in the linear viscoelastic region (LVR) [20], that was determined by a dynamic oscillation test. This test consists on applying increasing cyclic levels of stress and strain at a constant frequency. The point at which a dynamic viscoelastic function (either G^* or η^*) deviates by more than 10% from a constant value indicates departure from linear viscoelastic behaviour [21,22]. Both the storage modulus (G') and loss modulus (G'') versus shear stress (τ) were plotted and the LVR was determined as previously explained.

Amplitude sweep tests were performed using a shear stress (τ) between 0.005 and 100 Pa, shear strain (γ) oscillating in a range of 0.01–100% and a constant angular frequency (ω) of 10 rad/s. The flow curves were obtained by applying a linear ramp of γ starting from 0.1 to 100 Hz. The oscillatory frequency sweep measurements were performed using a fixed γ = 0.2% and a ω ramp between 0.1 and 500 rad/s.

To describe the thixotropic behaviour of the hydrogels, which is a time-dependent non-Newtonian behaviour of some fluids, a "three interval thixotropy test" (3-ITT) was performed. Firstly, the samples were exposed to a constant shear rate of 0.25 Hz for 50 s. Afterwards, the shear rate was heavily increased to 1000 Hz for 10 s. As a last step, the shear rate was set again at 0.25 Hz and maintained for 100 s until the end of the experiment. The differences in viscosity between the alternating shear rates are known as the thixotropic recovery, being the thixotropic time the total interval for a previously defined recovery percentage. Experiments were conducted twice with n = 3 samples.

2.3. Fourier transform infrared spectroscopy (FTIR) of the membranes

Previously dried and ground membranes (M-0, M-0.11, M-0.55 and M-1.1) were homogenised with 1% w/w KBr (FTIR grade, 99%, Sigma-Aldrich, ref. n. 221864). The mixture was further dried at 40 °C for 48 h and placed on a microsample cup. The characterization was performed using a Fourier transform infrared spectroscopy (FTIR, NICOLET Nexus 470) with an AVATAR Smart Diffuse Reflectance accessory. The measurements were done at 2 cm^{-1} resolution and 64 scans min^{-1}. The KBr spectrum was collected and subtracted from the samples' spectra.

2.4. Mechanical properties of the membranes

The membranes were cut into strips to a width of 10 mm. The Young modulus (E), maximum tensile stress (σ_{max}), maximum tensile strain (ε_{max}), yield stress (σ_y) and yield strain (ε_y) were mea-

sured along the longitudinal direction in an Instron Universal Testing Machine (Model 3369) using a 1 kN load cell at a strain rate of 0.01 mm s^{-1} and an initial gap separation of 5 cm. Experiments were conducted with n = 6 samples.

Maximum tensile stress was calculated by dividing the maximum load required to break the membrane by the cross-sectional area. Maximum tensile strain was calculated by dividing the membrane elongation at rupture by its initial length and multiplying by 100. Resilience modulus (Eq. (1)) [23] and plasticity (Eq. (2)) [24] were gauged based on the classic parameters:

$$\text{Resilience modulus} = \int_0^{\varepsilon y} \sigma d\varepsilon \text{ assuming linear elastic region}$$

$$\text{Resilience modulus} = \sigma y^2/2E \qquad (1)$$

$$\text{Plasticity} = (\sigma_{max} - \sigma_y)/\sigma_{max} \qquad (2)$$

2.5. In vitro degradation under physiological conditions

Membranes degradation was evaluated through a gravimetric assay using an analytical balance (Radwag AS220/C/2) with a sensibility of 0.1 mg. The membranes were weighted (w_0) and placed in Petri dishes with 3 mL of phosphate buffer solution (PBS, pH 7.4, Sigma Aldrich, ref. n. 806552) supplemented with 0.02% w/v sodium azide as bactericidal agent. The membranes were immersed in PBS at 37 °C for 168 h, refreshing the solution every day to prevent saturation. At each time point, samples were carefully washed with distilled water to remove adsorbed ions and afterwards dried at 37 °C until constant weight (w_t). Experiments were conducted with n = 5 samples. The degradation of the membranes was directly related to the rate of weight loss (% w_L), which was calculated following Tampieri et al. [25] methodology (Eq. (3)):

$$\%w_L = \frac{(W_0 - W_t)}{W_0} \times 100 \qquad (3)$$

2.6. Surface characterisation of the membranes

The surface characterization of each side of the membranes was performed using a Field Emission Scanning Electron Microscope (FE-SEM, Zeiss Ultra Plus) coupled to an X-ray energy-dispersive (EDX) spectrometer. The accelerating voltage (EHT) applied was 20 kV with a working distance (WD) of 8.5 mm. Local compensation of charge was achieved by injecting nitrogen gas.

The pore sizes of the surface and the size of the microaggregates of HAn were quantified from SEM microphotographs analysing between 50 and 110 measurements and an image visualization software (Image J 1.34s, NIH Image, USA) [26]. Roughness parameters, specifically the arithmetic average (R_a), skewness (R_{sk}, asymmetry coefficient) and Kurtosis (R_{ku}, "tailedness" coefficient), were determined in the same visualization software using a surface area of 1000 μm^2.

2.7. Cell culture assays

To test if the bilayered membrane would promote both bone regeneration and wound healing, osteoblast and fibroblasts cell were seeded on the mineral-rich side (MS) and the fibrous side (FS), respectively. Human osteoblast-like Saos-2 cells (ATCC) and human dermal fibroblasts (hDF) (ECACC) were cultured in flasks in an incubator with a humidified atmosphere of 5% CO_2 in air at 37 °C. Saos-2 were cultured in McCoy's 5A medium (Thermofisher Scientific, ref. n. 16600082) supplemented with 15% fetal bovine

serum (FBS, Gibco, ref. n. 16000044), whereas hDF cells with MEM/F12 medium (Fisher Scientific, ref. n. 11320082) supplemented with 10% FBS. Both media were also supplemented with 1% penicillin-streptomycin. The medium was changed every other day. Upon 80% confluence, cells were detached with a minimum amount of TrypLE Express (Gibco, ref. n. 12604039), which was inactivated with complete medium after 5 min. The cells were then recultured or used for the experiments. All experiments were done with Saos-2 within passages 16–18 and hDF at passage 4.

The membranes were cut in circular shapes (8 mm diameter) using a biopsy punch (WPI, USA). Afterwards, they were sterilized by being exposed to a UVC lamp (254 nm) for 15 min on each side. The membranes were placed into the bottom of a 48-well plate with either the MS facing up when culturing osteoblasts Saos-2 cells, or with the FS facing up when culturing hDF cells. Since the membranes were very light, a support was needed to ensure that they would remain in place when seeding and culturing the cells [27,28]. For this reason, ethanol-sterilized cyclic olefin copolymer (COC)-rings (6 mm inner diameter and 8 mm outer diameter) were placed on top of the membranes (Fig. 1).

Before cell seeding, the membranes were preincubated with 50 μl of 5 μg/cm^2 fibronectin (Gibco, ref. n. 33010-018) for 2 h to promote initial cell attachment (Fig. 1b). Afterwards, cells were seeded on the membranes using a low volume to minimize cell adhesion on the well plate. A drop of 50 μl of cell suspension 1.5×10^6 cells/ml (expected 25,000 cells/cm^2 on each membrane) was added (Fig. 1c). After 6 h of cell seeding, 300 μl complete medium was added into each well plate. The media was carefully refreshed every other day to ensure an adequate source of cell nutrients and waste removal (Fig. 1d). Cells cultured in the same density on tissue culture treated polystyrene (TCPS) of well plates served as controls. Each sample was evaluated in triplicate and the entire experiment was performed twice with Saos-2 and once with hDF. Increasing cell densities were cultured on TCPS for 24 h and quantified to generate a standard curve, which allowed to transform the measured signals to cell numbers.

2.7.1. Osteoblasts and fibroblasts proliferation

Saos-2 cells were cultured for 3, 7 and 14 days and hDF for 2 and 5 days. PrestoBlue assay (Invitrogen, ref. n. A13262), a resazurin-based solution, was used to monitor and quantify cell proliferation. Resazurin is a non-cytotoxic and redox-sensitive dye that is irreversibly reduced to fluorescent resorufin by aerobic respiration of metabolically active cells. PrestoBlue 10% v/v was diluted in transparent medium (MEM alpha, Thermofisher,

ref. n. 41061029) and was added into the well, which were previously washed with PBS. After 1 h incubation, fluorescence was analysed on a microplate reader (Tecan Infinite M200®) using a fluorescence excitation wavelength of 560 nm and a fluorescence emission of 590. One experiment was conducted for hDF and two full experiments were performed for Saos-2, using triplicates in each experiment.

2.7.2. Osteoblasts differentiation

At days 7 and 14, cells were washed with PBS and then lysed with 0.1% v/v triton X (Sigma-Aldrich, ref. n. X100) diluted in PBS. As per manufacturer's instructions, alkaline phosphatase activity (ALP) in the lysate was assessed using an alkaline phosphatase yellow p-nitrophenylphosphate (pNPP) liquid substrate system for ELISA (Sigma-Aldrich, ref. n. P7998). The yellow reaction product was read at 405 nm on a Tecan Infinite M200® microplate reader. ALP activity was normalized to the incubation time prior the measurement and the lactate dehydrogenase (LDH) protein absorbance (490 nm–690 nm). Experiments were conducted twice with including triplicate samples.

2.8. Statistical analysis

Results are presented as mean ± standard deviation. Statistical analysis was done in Excel (Microsoft corporation, USA) using two-tailed Student's unpaired sample t-test at a significance level of α = 0.05 (*) or α = 0.01 (**).

3. Results and discussion

Guided bone regeneration membranes must fulfil a series of properties to be successful, including good mechanical performance, steady biodegradation and promotion of tissue regeneration. In this work, through the combination of two well-known biocompatible materials such as ALG and HAn, novel bilayered membranes were developed. The influence of different amounts of HAn in the mineral-rich side of the membranes was analysed through several physico-chemical properties. Moreover, the ability of each membrane side to influence cells behaviour was determined in an attempt to predict their tissue-specific regeneration capability.
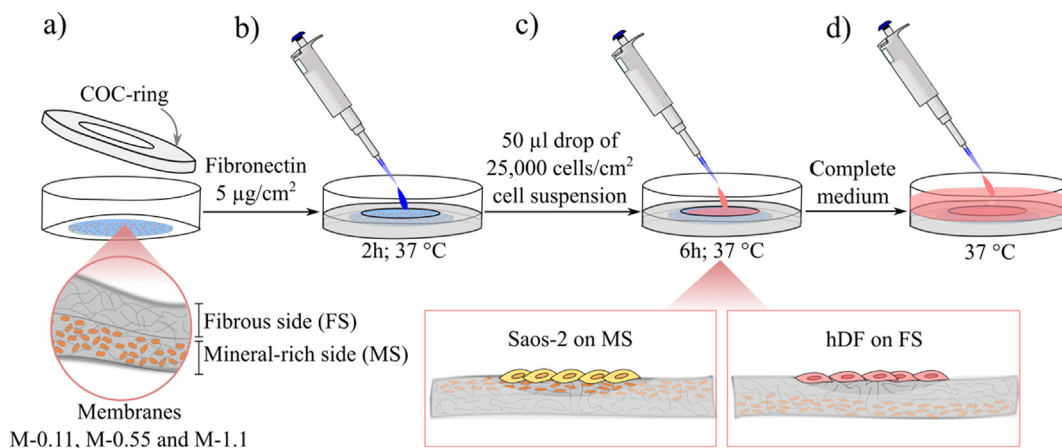
Fig. 1. Scheme of the general protocol followed for cell seeding. (a) First the membrane and then a COC-ring were placed into the well; (b) fibronectin (5 μg/cm^2) was added and placed into the incubator for 2 h, (c) a drop of cells suspension in a high density (25,000 cells/cm^2) was seeded, either with the MS facing up for Saos-2 or the FS facing up for hDF. Cells were allowed to attach for 6 h. (d) Finally, complete medium was added and the cells were analysed at the established time points.
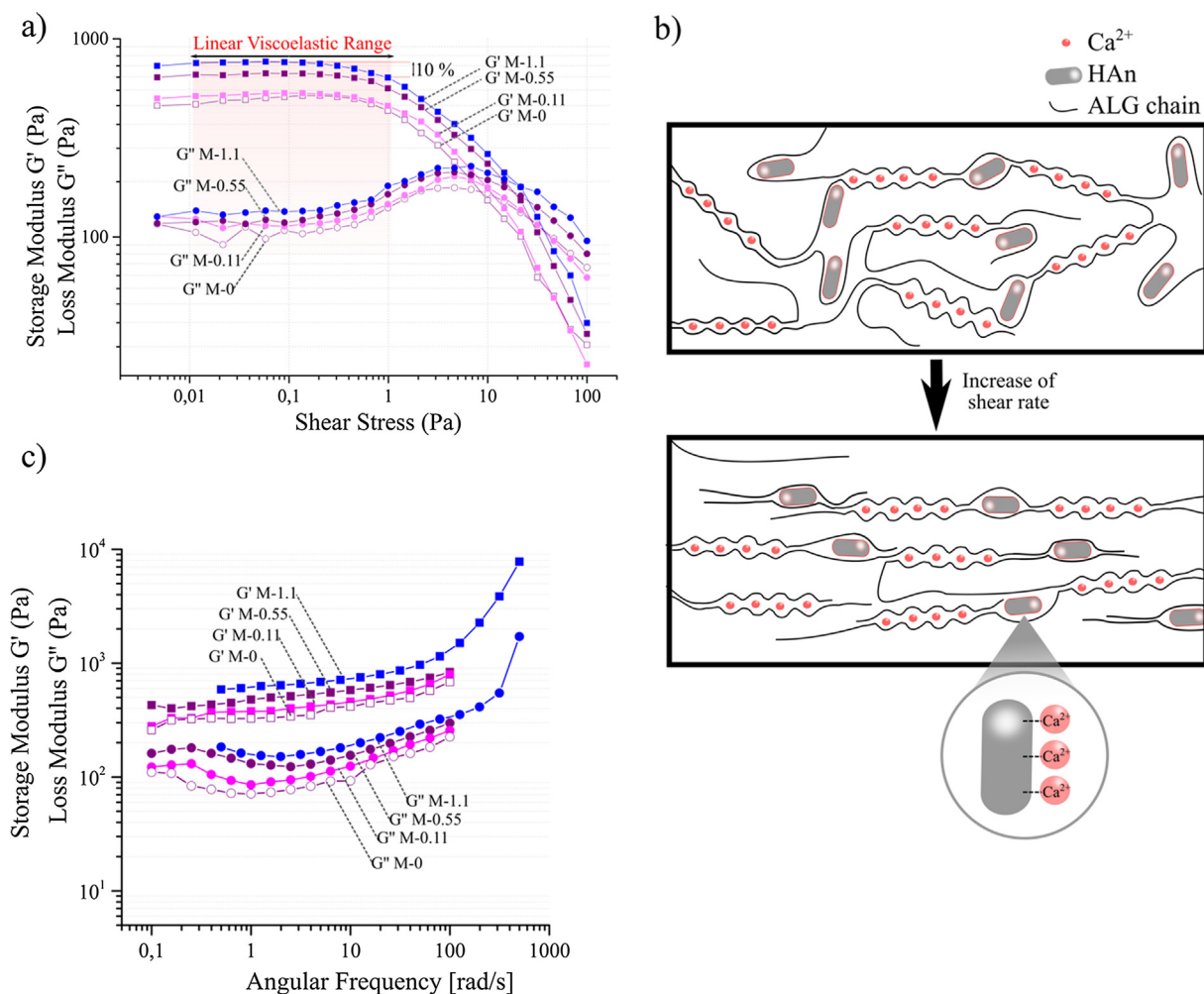
Fig. 2. (a) Amplitude sweep for hydrogels M-0, M-0.11, M-0.55 and M-1.1, (b) scheme representing the alignment of HAn within the hydrogel along the streamline when shear rate increases. The ALG-Ca^{2+} and ALG-HAn interactions are also represented, (c) frequency sweep when a controlled deformation (γ = 0.2%) was applied.

3.1. Study of alginate - nanohydroxyapatite interaction

Rheological characterization of hydrogels is essential to understand the relationship between hydrogels' microstructure and their physical properties such as strength. Therefore, this characterisation is able to shed light on important phenomena such as the gel-like behaviour, the inner organization of the structure when shear stress is applied or the thixotropic nature of the films.

The linear viscoelastic range (LVR) of the hydrogels was evaluated performing amplitude sweep measurements. The LVR, which indicates the range where both the storage modulus (G′) and the loss modulus (G″) are independent of the applied deformation [20], meaning that the hydrogel structure is preserved, was shown to be between 0.01 and 1 Pa (Fig. 2). In this region, the G′ values had a direct relationship with the amount of HAn added in the hydrogels, with values from 490 and 750 Pa. The G′ represents the energy stored in the elastic structure of the sample and is usually associated with the strength of a material. Therefore, a higher strength could be ascribed to those hydrogels with a higher concentration of HAn and, in turn, with higher calcium levels. These results were in agreement with a previous work that reported that G′ values were increased with higher concentration of calcium ions in ALG hydrogels due to the crosslinking ability of this ion [29]. Likewise, the amount of HAn also played a fundamental role in the elasticity/stiffness of the hydrogels, since this property is directly related to the water present in the samples. The capability

of the hydrogels to absorb and integrate water is regulated by an equilibrium between the osmotic pressure and the elasticity of the hydrogel. In other words, the higher amount of water absorbed by the hydrogel the larger its elasticity becomes, causing an increase in osmotic pressure that hinders the absorption of more water. The addition of HAn caused a notable decrease in the amount of water and, consequently, increased hydrogels' stiffness, in agreement with previous studies [30].

The loss modulus (G″) was shown to be lower than the storage modulus (G′) (Fig. 2), which is characteristic of a gel-like behavior. G″ is related to the portion of the deformation energy that is lost by internal friction when a shear is applied. It can be assumed that at low shear rates, the structure of the hydrogel was maintained, with few individual bonds breaking in the network. When the shear is greater than the strength of the network, active ALG-HAn junctions are destroyed and the internal structural architecture of the gel starts to break down. Consequently, the G″ became higher than G′, and the gel started to flow. The G′ and G″ of all hydrogels converged in the range between 10 and 30 Pa (flow point). At higher shear stresses, the values of G′ and G″ decayed abruptly (Fig. 2a) due to the ability of HAn and HAn-clusters to align along the streamlines (Fig. 2b), leading to a reduction of the flow resistance. Furthermore, the increment in the thermal agitation and the decrease of the viscosity could possibly facilitate the arrangement

of the HAn. A similar conclusion was reached in another work that modelled the behavior of rods in a polymer solution [31].

The oscillatory frequency sweep measurements provided information on the behaviour and inner structure of polymers as well as on the long-term stability of dispersions. The viscoelastic properties of the hydrogels had an exponential relationship with the frequency in the range between 1 and 400 rad/s (Fig. 2c). These results were analogous to those achieved measuring soft glassy materials with a gel structure [32].

Flow curve graphs allowed to study the relationship between shear stress and shear rate of the hydrogels. The shear stress increased exponentially when the shear rate rose (Fig. 3a), providing that the hydrogels had a shear thinning behaviour, which is typical of polymer solutions, complex fluids and suspensions. Moreover, the relationship between shear stress and viscosity of the hydrogels was also evaluated. In this case, all hydrogels showed a rapid viscosity descent as the applied stress increased and started to stabilize around a shear rate of 20 s^{-1} (Fig. 3b). The fall on the viscosity could be caused by the rupture of ALG-HAn chains within the hydrogel net. As observed in the most stable region (40–100 s^{-1}), the viscosity was HAn dependent, being the viscosity sensitively higher as the concentration of nanoparticles increased. This behaviour was in good agreement with the previously analysed amplitude sweep measurements. Presumably, a larger concentration of HAn resulted in the formation of more ALG-HAn interconnections, i.e. increasing the length and ramifications of the polymer network, which increased the strength and viscosity of the hydrogel. As it was previously inferred from the dependence of both G' and G'' with the frequency, this rheological behaviour could correspond to a soft glass material [33].

Finally, a 3-ITT test was performed to evaluate the thixotropic behaviour of the hydrogels. Thixotropy is generally characterized by a decrease in the viscosity or G' as a result of a mechanical load, and a total or partial recovery of the initial state when the load is reduced [29]. Fig. 4 shows that the four hydrogels had a similar behaviour when a low shear rate was applied, with constant viscosity values between ~50,000 and 80,000 mPa·s. After this first interval, the shear rate was increased heavily enough to destroy the internal network of the materials, causing a dramatic decrease in viscosity to around 400–800 mPa.s. Reversely, when the shear was ceased, the viscosity of all hydrogels was recovered ~90%, which is a reasonable thixotropic recovery value for this type of materials [29]. The rate of disentanglement by shearing was slightly higher than of re-entanglement, partially caused by the alignment of the polymer chains along the direction of the shear
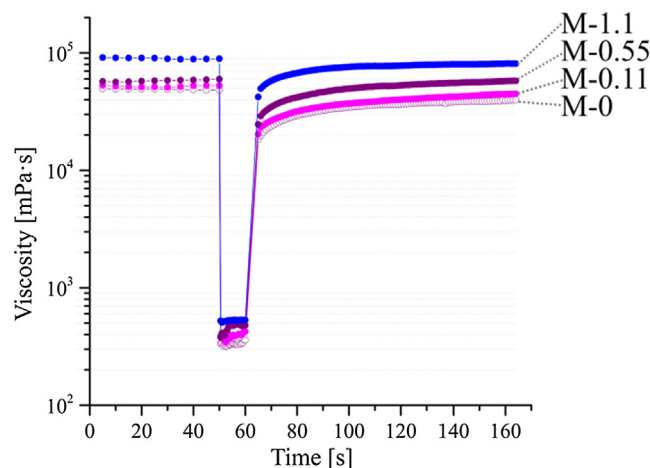

Fig. 4. Three-step thixotropy test (3-ITT) of the membranes M-0, M-0.11, M-0.55 and M-1.1.

and proving the thixotropic behaviour of the films, typical characteristic of most hydrogels [29].

In order to support rheological results in the hydrogels, the membranes were studied by Fourier transform infrared spectroscopy (FTIR), an essential technique for assessing the chemical interaction between ALG and HAn. The spectra obtained for the HAn-free membrane (M-0) and the HAn-containing membranes (M-0.11, M-0.55 and M-1.1) are showed in Fig. 5a. Alginate membranes without HAn (M-0) displayed bands at 1616 and 1413 cm^{-1} that can be attributed to asymmetric and symmetric stretching vibrations, respectively, of ionized carboxylic group (COO^-) on the polymeric backbone characteristic of ALG. The bending of the OH^- group of the carboxyl is depicted at 1303 and 818 cm^{-1} [34]. Interestingly, consistent differences were observed on the bands of the spectrum corresponding to M-0 (only ALG) in comparison with the membranes containing HAn (Fig. 5b). Specifically, the two ALG bands at 1616 and 1413 cm^{-1} were shifted and their intensity decreased in M-0.55 and M-1.1 spectra, whereas it was difficult to identify them in M-0.11. On the other hand, the bands at 1303 and 818 cm^{-1} disappeared in all the HAn-containing membranes. This effect was previously observed in ALG-HAn composites [35,36] and could be attributed to the bonding formed between Ca^{2+} present on the HAn surface and the oxygen sites of
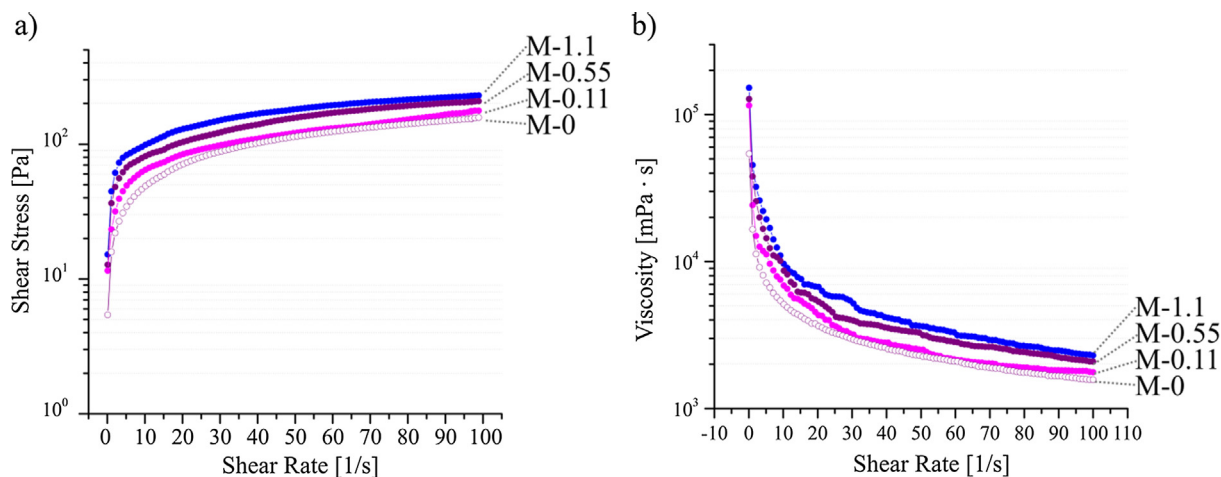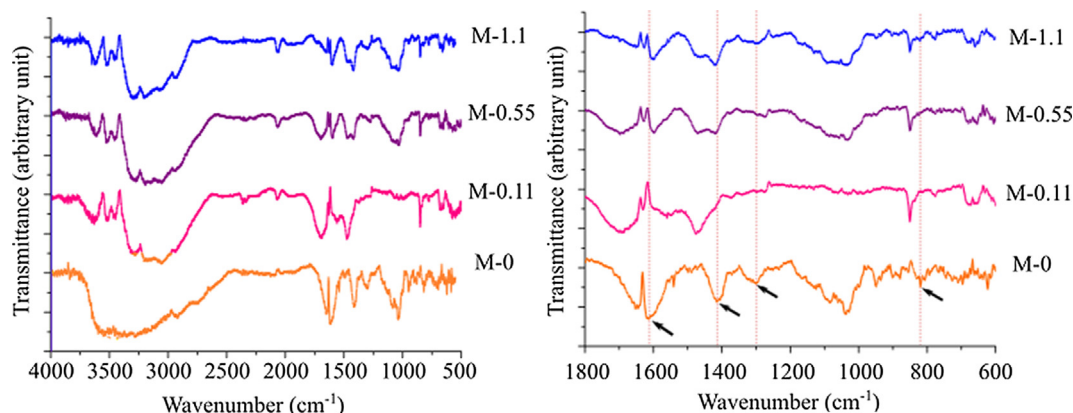

Fig. 3. (a) Shear stress vs. shear rate and, (b) viscosity vs. shear rate of the membranes M-0, M-0.11, M-0.55 and M-1.1.

Fig. 5. FTIR spectra of membranes M-0, M-0.11, M-0.55 and M-1.1, (a) broad range 500–4000 cm^{-1}, (b) magnification between 1800 cm^{-1} and 600 cm^{-1} is displayed. The arrows indicate characteristic ALG bands attributed to carboxylic groups (COO$^-$) in the wavenumbers 1616 and 1413 cm^{-1}, and hydroxyls (OH$^-$) from the carboxylic groups in 1303 and 818 cm^{-1}.

COO$^-$ groups of ALG [37]. These results support the fact that the incorporation of HAn contributed in the hydrogels strength as shown in the rheology analysis.

3.2. Mechanical performance of the membranes under tensile strength

Adequate mechanical properties are essential for membranes aimed for GBR applications, since these properties determine their clinical handling during implantation as well as its performance once in place. Strain-stress curves, obtained by the tensile test of the membranes, were evaluated regarding their parameters in the elastic region, yield point and plastic region (Fig. 6).

An important parameter of the elastic region is the Young modulus (E), a mechanical property that measures the stiffness of a solid material. It indicates the relationship between shear stress and shear strain in the elastic region, where the deformation is still reversible. This parameter was slightly influenced by the presence of HAn, and a statistically significant difference was only found between M-0.11 and M-1.1 (p = 0.003) (Fig. 7a). The maximum E values were reached with M-0.11 and M-0.55, suggesting that 0.11 and 0.55% HAn led to the highest crosslinking interactions
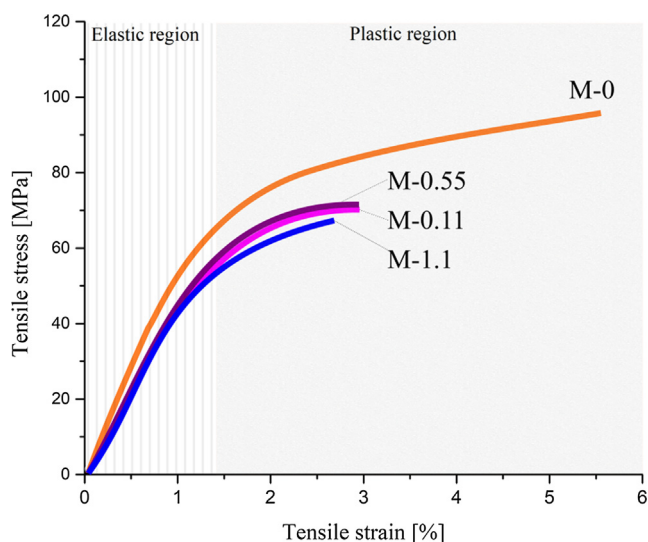

Fig. 6. Representative stress-strain curves of the membranes M-0, M-0.11, M-0.55 and M-1.1 showing the approximate location of elastic region, yield point and plastic region.

for the selected ALG concentration (2% w/v). Interestingly, these E values (~5–6 GPa) were higher than other membranes aimed to similar applications [38,39], and were comparable with E of cranial bone (E ~ 5–18 GPa) [40]. This is important since it is well known that E of a biomaterial should closely match with the E of the host tissues to avoid mechanically compromising the site. In fact, it was proved that a significant difference between the E of a biomaterial and that of the surrounding tissue could lead to mechanical stress resulting in encapsulation, inflammation and the final failure of tissue regeneration [41].

Continuing with the elastic region of the stress-strain curves, the resilience modulus, which represents the energy required to stress the material from the zero stress to the yield stress point, showed no significant differences among the three HAn-containing membranes values between 0.17 MPa and 0.20 MPa) (Fig. 7a). These results indicated that the resilient nature of the membranes was not affected by the amount of HAn added. This is worth to consider because resilience, which was also acknowledged by the membranes' capability to recover their original structure after handling, is needed in order to facilitate membrane placement during surgical procedures. Nevertheless, as expected, due to the crystal nature of HAn [17] (Fig. S.M. 1), the resilience modulus of M-0 was significantly higher than those found in the HAn-containing membranes (p values indicated in Table S.M. 2). It is important to consider that these results showed that all the HAn-containing membranes tested have a similar behaviour in the elastic region of the stress-strain curves despite of the immersed HAn crystals.

Increasing the stress above the threshold that begins to cause permanent damage to the membranes structural integrity allowed to obtain information about the yield point (Fig. 7b). The yield stress (σ_y) values of all the membranes, which were between 33.8 MPa and 63.0 MPa, exceed to those obtained for human trabecular bone (1.7 MPa) under tensile load [42]. In contrast, the yield strain (ε_y) values of all membranes (between 1.0% and 1.4%), were comparable with the trabecular (0.8%) [42] and cortical bone (0.6−0.9%) [43].

In the plastic region, the maximum tensile strain (ε_{max}) and the maximum tensile stress (σ_{max}) were evaluated. These two intimately related parameters that can be interpreted as the deformation percentage of the membranes at the breaking point (ε_{max}) and the highest load supported (σ_{max}), respectively, showed an indirect correlation between maximum load and HAn concentration. In the case of ε_{max}, the obtained value of M-0 was ~ 5.5% when a σ_{max} ~ 98 MPa was applied. In contrast, HAn-free membrane (M-
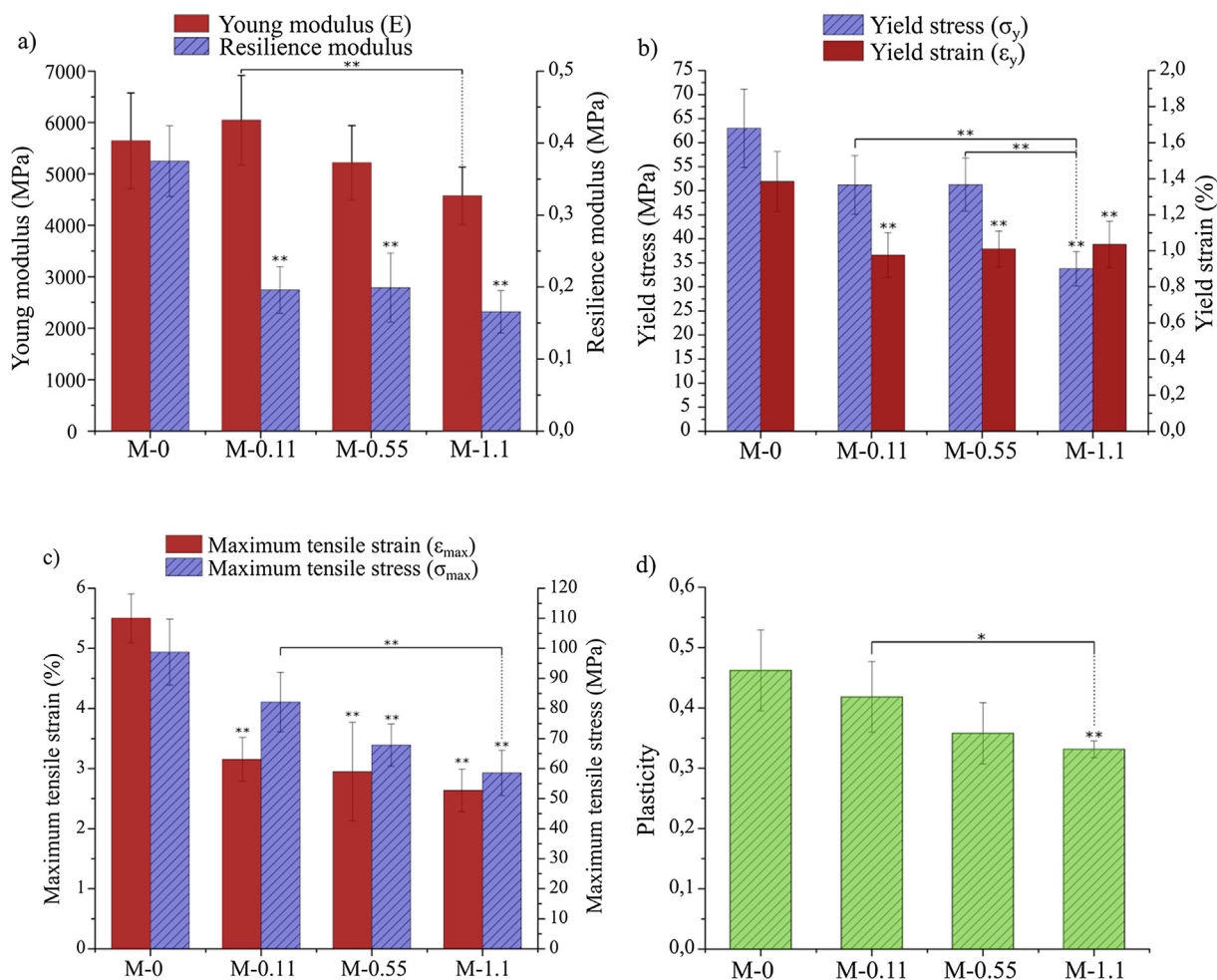
Fig. 7. Tensile assay parameters of membranes M-0, M-0.11, M-0.55 and M-1.1. (a) Elastic region: Young modulus and resilience. (b) Yield point: yield stress and yield strain. (c) Plastic region: maximum tensile strain and maximum tensile stress and, (d) plasticity. Significant differences between HAn-containing membranes and M-0 are indicated on the top of the column, while between the HAn-containing membranes with brackets. Significance: *p < 0.05 and **p < 0.01.

0) had a statistically higher ε_{max} than the three HAn-containing membranes, while among σ_{max} values only M-0.11 was statistically significantly higher than M-1.1 (Fig. 7c) (p values indicated in Table S.M. 2). The ε_{max} of M-0.11 and M-0.55 was ~ 3% when a σ_{max} of ~ 75 MPa was applied, and for the membranes with the highest HAn content (M-1.1) both the tensile strain and the tensile stress were reduced even further (~2.6% when ~ 63 MPa was applied). In spite of this fact, the ε_{max} were comparable or lower than other membranes applied to GBR [39,44]. Interestingly, all the σ_{max} parameters determined were higher than those found in the trabecular bone of human mandible, which have been ranged between 0.2 and 10.4 MPa [45]. Plasticity, which refers to the permanent deformations made to the materials, is another parameter of the plastic region. In this particular case, M-0 and M-0.11 had a statistically significant higher plasticity than M-1.1 (Fig. 7d) (p values indicated in Table S.M. 2).

In summary, the presence of HAn affected the tensile strength of the membranes, without major differences among HAn-containing membranes. This performance may be due to the presence of the nanoparticles, which are highly ordered structures and once introduced in an amorphous conformation such as ALG could generate failure points. In addition, as previously described in the rheological studies of the hydrogels, the presence of HAn particles reduced the capacity of hydrogels to absorb water, making them less flexible. As water acts as a plasticizer of polymers [46], its

decrease in the membranes together with the presence of HAn could synergically make the membranes more rigid. Similarly, the increment in stiffness generated by the presence of HAn
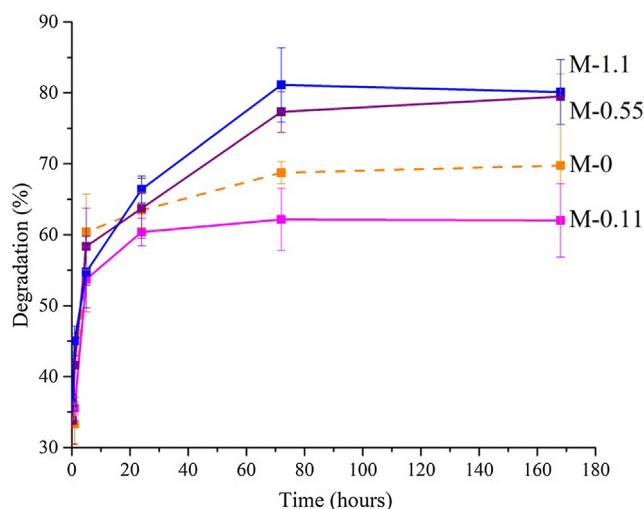
Fig. 8. Degradation over time of the membranes M-0, M-0.11, M-0.55 and M-1.1 immersed in PBS at 37 °C.

nanoparticles was previously reported for chitosan-HAn [47,48], chitosan-glass nanoparticles [49] and polycaprolactone-glass microparticles [50].

3.3. Degradation under in vitro physiological conditions

The degradation behaviour of the membranes immersed in PBS is shown in Fig. 8. During the first 24 h, all membranes had a similar degradation rate, with a quick degradation of ~ 60–66%. Between 24 h and 72 h, a steady degradation was observed for M-0.55 and M-1.1 (degradation ~ 77–81%), whereas M-0 and M-0.11 slowed down their degradation (degradation ~ 62–69%). None of the membranes seem to degrade any further between 72 h and 168 h. At the last time-point of immersion, 168 h, the degradation of M-0.11 was ~ 62%, significantly lower than both M-0.55 and M-1.1 in PBS (p = 0.004 and 0.01, respectively). However, there were no differences between the two membranes with the highest amount of HAn (M-0.55 and M-1.1). At the last time-point, the degradation for M-0 (69 ± 13%) was in-between the two groups of HAn-containing membranes (~62–80%).

The degradation decreased in the membranes with the lowest amount of HAn (0.11% w/v), since the chemical interaction between ALG and HAn was enhanced. In contrast, higher concentrations (0.55 and 1.1% w/v) promoted degradation, which could be attributed to the instability generated in the structure by the crystalline phase. Moreover, as the HAn amount increased, a higher number of HAn aggregates were also formed. These aggregates create instability in the ALG-HAn structure and contribute to the degradation process. This correlates well with the results of the tensile assays, where HAn aggregates compromised the mechanical performance of the membranes in the plastic region, as they increased the rigidity of the membranes and in turn generated failure points. The steady degradation over time observed for all the samples increase the potential of these membranes for GBR applications. This would, on one hand, provide space for the newly formed bone tissue and, on the other hand, avoid a second surgical procedure for extracting the membrane.

3.4. Surface characterisation each side of the membrane

It is well known that surface characteristics of biomaterials deeply affect cell behavior, influencing adhesion, proliferation and differentiation [51]. Micrographs displaying both FS and MS surface of M-1.1 (the membrane with maximized chemical differences between both sides) are shown in Fig. 9a–d. The FS showed a highly porous structure, with pore sizes varying from 19 μm to 150 μm with a mean value of 65.9 ± 28.0 μm (Fig. 9e). On one hand, pores ~ 100 μm are usually considered advantageous to achieve an adequate vascularization of the tissue being repaired [52]. On the other hand, pores smaller than ~ 40 μm can prevent infiltration of unwanted cells [53]. Therefore, the porosity of the FS surface could be expected to allow transport of oxygen and nutrients, irrigation and blood vessels formation, while migration would probably be hindered since no specific methodology was used to promote pores interconnectivity throughout the membrane.

The MS surface exhibited lower pore density than the FS one (Fig. 9a,b). A similar result was previously shown on chitosan-HAn membranes [5], where the addition of HAn reduced the biomaterial porosity. The lower pore density observed in the MS surface could be attributed to the effective crosslinking interactions between HAn and ALG chains, reinforcing the membrane structure. The bonding between ALG molecules and HAn had an immediate effect not only on the microstructures of the membranes, but also in the chemical interaction of the hydrogels [54]. Therefore, it can be hypothesized the ALG chains were successfully grafted on HAn surface, making the biomaterials ordered at the nanoscale range.

In addition, HAn microaggregates measuring 2.51 ± 0.65 μm dispersed all over the MS surface were observed (Fig. 9c,d). These aggregates are expected to promote the bioactivity of the membranes due to their capability to nucleate and grow calcium phosphate crystals in contact with physiological fluids. As it is well known, this could further stimulate bone regeneration [55]. Moreover, the HAn microaggregates would increase the surface area on the MS, enhancing its bioactivity as well as increasing chances for protein entrapment, essential processes for the osteoblasts adhesion [56]. Consequently, the HAn microaggregates randomly distributed could be expected to enhance discontinuous bone ingrowth. This effect has been correlated with an enhanced osteogenesis since bone would form not only from the margins, but also throughout the whole area [57,58].

The roughness analysis performed with SEM micrographs was in accordance with the microstructure imaged. The porous FS surface resulted in statistically lower values for both R_a and R_{sk} (p ≤ 0.01) than the MS surface, which had a lower pore density (Fig. 10). An appropriate surface roughness can produce beneficial interlocking of the cells at the initial adhesion stage and improve cell adhesion. The asymmetry coefficient (R_{sk}) used to study the symmetry of the roughness profile over the midline, was positive for both FS and MS, indicating profiles with a high shear resistance, where peaks predominate over valleys [59]. The kurtosis coefficient (R_{ku}) was used for the detection of sharp peaks and isolated deep valleys, since it describes the sharpness of the probability density of the profile [60]. This parameter was lower than 3 for both in MS and FS, meaning a platykurtic distribution of the profile curve, characteristic of profiles with few sharp peaks [60]. Previous studies have proved that the presence of a large number of sharp peaks ($R_{ku} > 3$) on the surface of biomaterials generates an increase in the concentration of stresses in the tissue-biomaterial interface [61], which could even lead to the failure of the biomaterial. Therefore, better responses are in general expected on surfaces with $R_{ku} < 3$, such as the ones found in both surfaces.

3.5. Cell culture

3.5.1. Osteoblast proliferation and differentiation on the mineral-rich side (MS) of the membranes

Osteoblasts were cultured on the MS of the membranes and their proliferation over time was evaluated using PrestoBlue, an indicator of metabolic active cells (Fig. 11a). At 3 days, no differences were found among membranes. The number of cells was significantly lower on membranes M-0.11 (p = 0.016) and M-0.55 (p = 0.041) compared to the TCPS (control), while there were no differences between M-1.1 and TCPS. At 7 days, there were no differences between any of the samples. At day 14, a statistically significant higher number of cells was observed on M-1.1 compared with M-0.55 and M-0.11 (p = 0.018 and 0.022, respectively), although no difference was shown between M-0.55 and M-0.11. Interestingly, M-0.55 and M-1.1 had a statistically higher number of cells than TCPS at day 14 (p = 0.003). The results showed that all membranes allowed osteoblasts proliferation and this effect seemed to be directly dependent on the amount of HAn present on the membranes. M-0 was not added as a control since good viability of osteoblasts on alginate has already been proved before [62].

The capacity of each membrane to stimulate the differentiation of osteoblast-like cells on MS was determined by ALP activity, an early marker of osteoblast differentiation that is expressed just before matrix mineralization begins. Results at 7 days manifested that there were no differences between the tested membranes and TCPS. However, at 14 days, cells showed a statistically superior ALP activity when cultured on M-1.1 compared to the other two membranes (p = 0.005 for both, M-0.11 and M-0.55) and TCPS
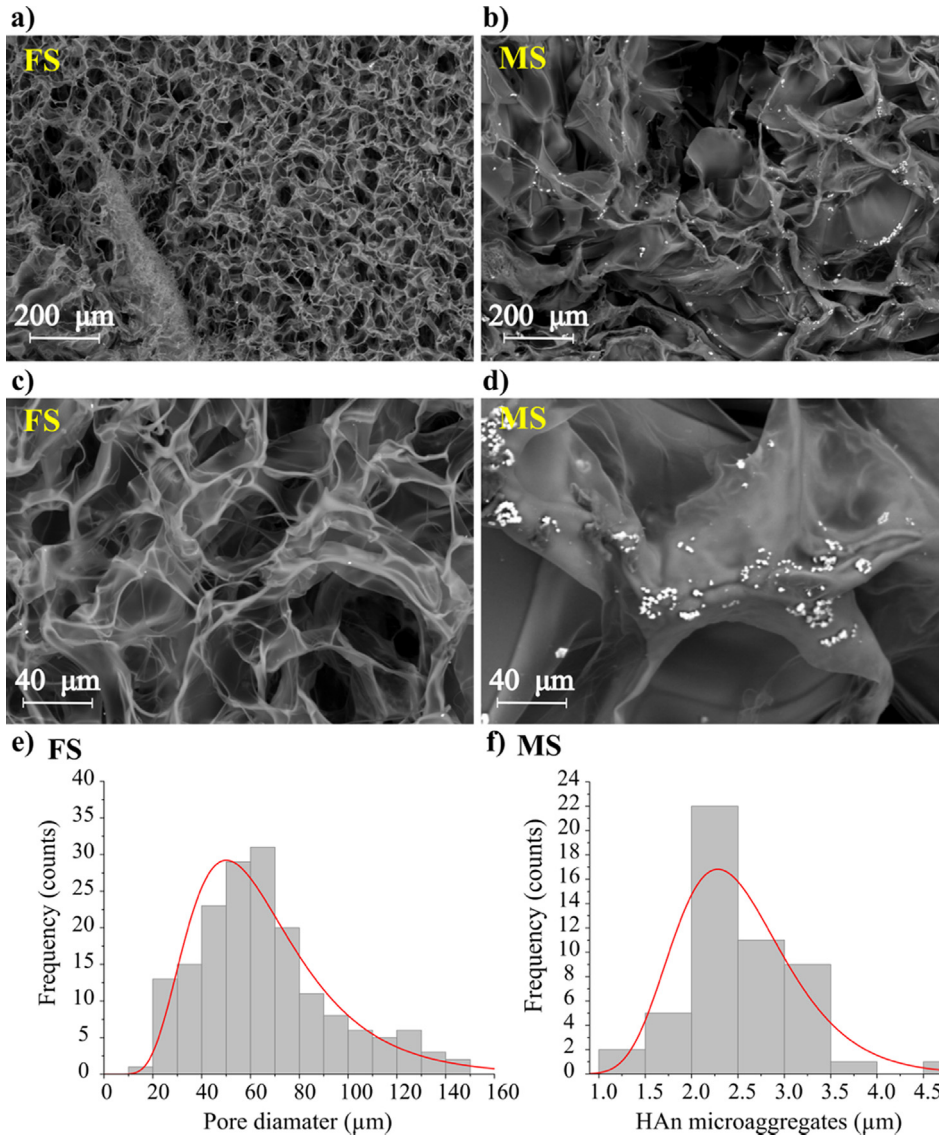
Fig. 9. Surface characteristics of M-1.1 membranes evaluated by SEM micrographs: (a) FS surface and (b) MS surface at a 200× magnification; (c) FS surface showing the porosity and (d) MS surface showing HAn microaggregates, at a 1000× magnification. Histograms displaying (e) pore size distribution of the FS surface and (f) HAn microaggregates size present on the MS.
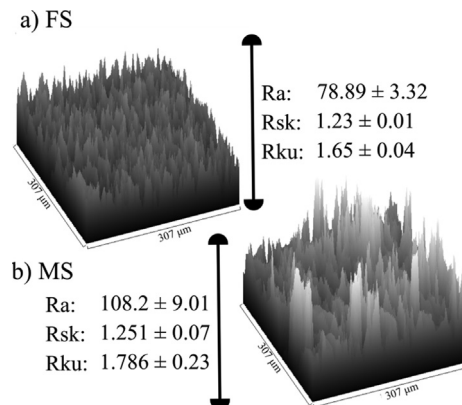

Fig. 10. Roughness parameters of M-1.1 membrane for the (a) FS and (b) MS. R_a: arithmetic average surface roughness, R_{sk}: asymmetry coefficient, R_{ku}: kurtosis coefficient.

($p = 0.007$). At the same time point, cells cultured on M-0.11 and M-0.55 did not show any differences compared to TCPS (Fig. 11b). These results confirm the osteogenic potential of HAn [16,18]. Specifically, a previous study found that a HAn coating induced the expression of specific markers involved in stem cell osteogenic differentiation [18].

3.5.2. Fibroblast proliferation on the fibrous side (FS) of the membranes

Fibroblasts (hDF cells) were cultured on the FS of the membranes to evaluate their growth over time. No differences were found between membranes at any time point. An increase in cell number along time was observed for all materials as well as for TCPS ($p = 0.003$, 0.048, 0.007 and 0.005 for, M-0.11, M-0.55, M-1.1 and TCPS, respectively). Compared with the TCPS, a statistically significant lower number of fibroblasts was determined for all the membranes at day 2 ($p = 0.0003$, 0.03 and 0.015 for M-0.11, M-0.55 and M-1.1, respectively) and at day 5 day ($p = 0.002$, 0.048 and
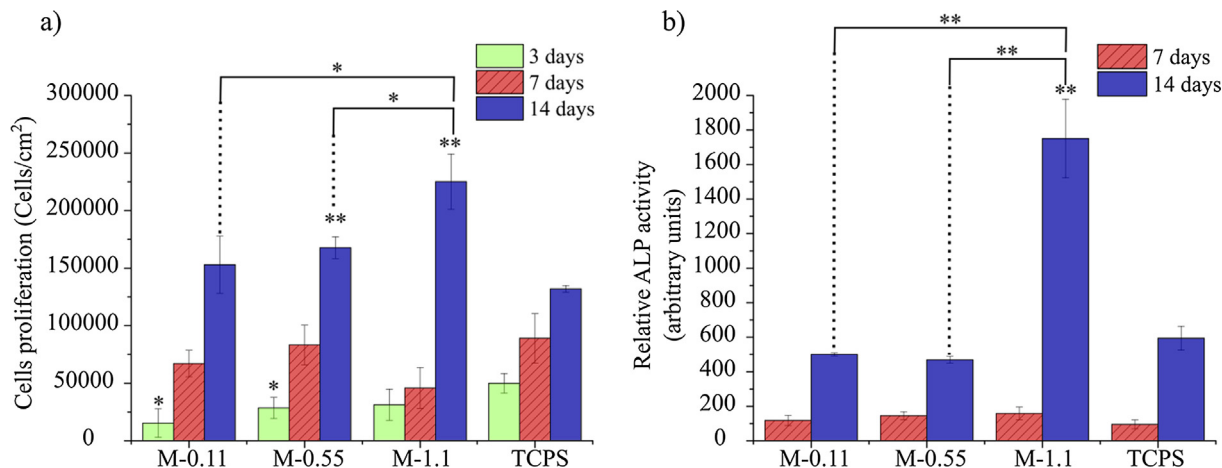
Fig. 11. Osteoblasts cultured on the MS of the membranes M-0.11, M-0.55 and M-1.1: (a) proliferation and (b) differentiation. TCPS was used as control. Significant differences between HAn-containing membranes and TCPS are indicated on the top of the column, while between the HAn-containing membranes with brackets. Significance: *p < 0.05 and **p < 0.01.
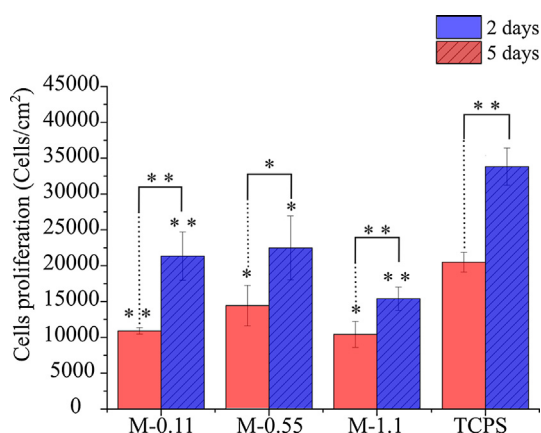
Fig. 12. Fibroblasts proliferation on the FS of the membranes M-0.11, M-0.55 and M-1.1. TCPS was used as control. Significant differences between HAn-containing membranes and TCPS are indicated on the top of the column, while between the 2 and 5 days with brackets. No differences were found between the HAn-containing membranes. Significance: * p < 0.05 and ** p < 0.01.

0.002 for M-0.11, M-0.55 and M-1.1, respectively) (Fig. 12). However, the control substrate used in this work, TCPS, was mainly used to determine an adequate cell growth rather than evaluating a fair comparison with membranes due to its different chemical and physical properties. Consistently, these results suggest that the fibroblast behaved similarly in all membranes regardless the HAn amount used during the crosslinking in the MS. The good viability of fibroblasts on alginate samples was already shown before [62].

4. Conclusion

In this work, we have designed a two-sided membrane that reproduces the structure and function of the periosteum. Alginate and diverse concentrations of nanohydroxyapatite were combined to develop bilayered membranes with a different chemical composition, roughness and porosity on each side. An efficient interaction between alginate chains and nanohydroxyapatite was found. A higher nanohydroxyapatite concentration increased the length and ramifications of the polymer networks and, in turn, decreased the amount of water in the structure. This resulted into an increase

in the viscosity and strength of the fresh hydrogel, while the plasticity of the membranes was reduced. The membrane was constituted by a highly porous fibrous side and a mineral-rich side with higher roughness, confirming its bilayered functionality. A favourable cellular response was observed for all the membranes tested, specifically growing osteoblasts on the mineral-rich side and fibroblasts on the fibrous side. Moreover, the membranes with the highest amount of nanohydroxyapatite significantly induced osteoblast differentiation. The physico-chemical properties of the bilayered membranes can be easily tuned, therefore providing versatility to meet the complex requirements of bone tissue engineering.

CRediT authorship contribution statement

Noelia L. D'Elía: Conceptualization, Investigation, Formal analysis, Methodology, Validation, Writing - original draft, Writing - review & editing. **Ramon Rial Silva:** Investigation, Methodology, Formal analysis, Validation, Writing - review & editing. **Javier Sartuqui:** Investigation, Formal analysis, Validation, Writing - review & editing. **Daniel Ercoli:** Methodology, Resources, Writing - review & editing. **Juan Ruso:** Conceptualization, Resources, Supervision, Writing - review & editing. **Paula Messina:** Conceptualization, Resources, Supervision, Writing - review & editing. **Gemma Mestres:** Conceptualization, Resources, Supervision, Methodology, Writing - original draft, Writing - review & editing, Funding acquisition, Project administration.

Declaration of Competing Interest

The authors declare that they have no known competing financial interests or personal relationships that could have appeared to influence the work reported in this paper.

Acknowledgements

Appendix A. Supplementary material

Supplementary data to this article can be found online at https://doi.org/10.1016/j.jcis.2020.03.086.

References

[1] M. Gong, C. Huang, Y. Huang, G. Li, C. Chi, J. Ye, W. Xie, R. Shi, L. Zhang, Core-sheath micro/nano fiber membrane with antibacterial and osteogenic dual functions as biomimetic artificial periosteum for bone regeneration applications, Nanomed. Nanotechnol. Biol. Med. 17 (2019) 124–136, https://doi.org/10.1016/j.nano.2019.01.002.

[2] D.W. Hutmacher, F. Wagner, L.C. Martine, B.M. Holzapfel, C. Theodoropoulos, O. Bas, F.M. Savi, E.M. De-Juan-Pardo, D.W. Hutmacher, Periosteum tissue engineering in an orthotopic in vivo platform, Biomaterials 121 (2017) 193–204, https://doi.org/10.1016/j.biomaterials.2016.11.016.

[3] I. Elgali, O. Omar, C. Dahlin, P. Thomsen, Guided bone regeneration: materials and biological mechanisms revisited, Eur. J. Oral Sci. 125 (2017) 315–337, https://doi.org/10.1111/eos.12364.

[4] A. Turri, I. Elgali, F. Vazirisani, A. Johansson, L. Emanuelsson, C. Dahlin, P. Thomsen, O. Omar, Guided bone regeneration is promoted by the molecular events in the membrane compartment, Biomaterials 84 (2016) 167–183, https://doi.org/10.1016/j.biomaterials.2016.01.034.

[5] S.B. Qasim, R.M. Delaine-Smith, T. Fey, A. Rawlinson, I.U. Rehman, Freeze gelated porous membranes for periodontal tissue regeneration, Acta Biomater. 23 (2015) 317–328, https://doi.org/10.1016/j.actbio.2015.05.001.

[6] A.I. Leal, S.G. Caridade, J. Ma, N. Yu, M.E. Gomes, R.L. Reis, J.A. Jansen, X.F. Walboomers, J.F. Mano, Asymmetric PDLLA membranes containing Bioglass® for guided tissue regeneration: Characterization and in vitro biological behavior, Dent. Mater. 29 (2013) 427–436, https://doi.org/10.1016/j.dental.2013.01.009.

[7] C. Song, S. Li, J. Zhang, Z. Xi, E. Lu, L. Zhao, L. Cen, Controllable fabrication of porous PLGA/PCL bilayer membrane for GTR using supercritical carbon dioxide foaming, Appl. Surf. Sci. 472 (2019) 82–92, https://doi.org/10.1016/j.apsusc.2018.04.059.

[8] T. Wang, Y. Zhai, M. Nuzzo, X. Yang, Y. Yang, X. Zhang, Layer-by-layer nanofiber-enabled engineering of biomimetic periosteum for bone repair and reconstruction, Biomaterials 182 (2018) 279–288, https://doi.org/10.1016/j.biomaterials.2018.08.028.

[9] S. Türkkan, A.E. Pazarçeviren, D. Keskin, N.E. Machin, Ö. Duygulu, A. Tezcaner, Nanosized CaP-silk fibroin-PCL-PEG-PCL/PCL based bilayer membranes for guided bone regeneration, Mater. Sci. Eng. C. 80 (2017) 484–493, https://doi.org/10.1016/j.msec.2017.06.016.

[10] D. Mao, Q. Li, D. Li, Y. Tan, Q. Che, 3D porous poly(ε-caprolactone)/58S bioactive glass–sodium alginate/gelatin hybrid scaffolds prepared by a modified melt molding method for bone tissue engineering, Mater. Des. 160 (2018) 1–8, https://doi.org/10.1016/j.matdes.2018.08.062.

[11] W. Paul, C.P. Sharma, Infection resistant hydroxyapatite/alginate plastic composite, J. Mater. Sci. Lett. 16 (1997) 2050–2051, https://doi.org/10.1023/A:1018564818186.

[12] M. Toda, K. Oshiro, H. Fujimori, S. Yamamoto, Fabrication of a novel bioceramic membrane for guided bone regeneration, J. Ceram. Soc. Japan. 114 (2006) 799–801. https://doi.org/https://doi.org/10.2109/jcersj.114.799.

[13] L. Benedini, D. Placente, O. Pieroni, P. Messina, Assessment of synergistic interactions on self-assembled sodium alginate/nano-hydroxyapatite composites: to the conception of new bone tissue dressings, Colloid Polym. Sci. (2017) 1–13, https://doi.org/10.1007/s00396-017-4190-x.

[14] L.A. Schneider, A. Korber, S. Grabbe, J. Dissemond, Influence of pH on wound-healing: a new perspective for wound-therapy?, Arch. Dermatol. Res. 298 (2007) 413–420.

[15] L.C. Parrish, T. Miyamoto, N. Fong, J.S. Mattson, D.R. Cerutis, Non-bioabsorbable vs. bioabsorbable membrane: assessment of their clinical efficacy in guided tissue regeneration technique. A systematic review, J. Oral Sci. 51 (2009) 383–400, https://doi.org/10.2334/josnusd.51.383.

[16] N.L. D'Elía, C. Mathieu, C.D. Hoemann, J.A. Laiuppa, G.E. Santillán, P.V. Messina, Bone-repair properties of biodegradable hydroxyapatite nano-rod superstructures, Nanoscale 7 (2015) 18751–18762, https://doi.org/10.1039/C5NR04850H.

[17] N.L. D'Elía, A.N. Gravina, J.M. Ruso, J.A. Laiuppa, G.E. Santillán, P.V. Messina, Manipulating the bioactivity of hydroxyapatite nano-rods structured networks: effects on mineral coating morphology and growth kinetic,

[18] Biochim. Biophys. Acta - Gen. Subj. 2013 (1830) 5014–5026, https://doi.org/10.1016/j.bbagen.2013.07.020.

[18] J. Sartuqui, C. Gardin, L. Ferroni, B. Zavan, P.V. Messina, Nanostructured hydroxyapatite networks: synergy of physical and chemical cues to induce an osteogenic fate in an additive-free medium, Mater. Today Commun. 16 (2018) 152–163, https://doi.org/10.1016/j.mtcomm.2018.05.010.

[19] A. Contreras-García, N.L. D'Elía, M. Desgagné, C.H. Lafantaisie-Favreau, G.E. Rivard, J.C. Ruiz, M.R. Wertheimer, P. Messina, C.D. Hoemann, Synthetic anionic surfaces can replace microparticles in stimulating burst coagulation of blood plasma, Colloids Surf. B Biointerfaces 175 (2019) 596–605, https://doi.org/10.1016/j.colsurfb.2018.11.066.

[20] A.R. Patel, P. Dumlu, L. Vermeir, B. Lewille, A. Lesaffer, K. Dewettinck, Rheological characterization of gel-in-oil-in-gel type structured emulsions, Food Hydrocoll. 46 (2015) 84–92.

[21] P. Astm International, West Conshohocken, ASTM D7175–08, Standard Test Method for Determining the Rheological Properties of Asphalt Binder Using a Dynamic Shear Rheometer, 2008.

[22] P. ASTM International, West Conshohocken, DIN 51810-2, "Testing of lubricants – Testing rheological properties of lubricating greases – Part 2: Determination of flow point using an oscillatory rheometer with a parallel-plate measuring system, (n.d.).

[23] M.E. Roy, L.A. Whiteside, J. Xu, B.J. Katerberg, Diamond-like carbon coatings enhance the hardness and resilience of bearing surfaces for use in joint arthroplasty, Acta Biomater. 6 (2010) 1619–1624, https://doi.org/10.1016/j.actbio.2009.10.037.

[24] J. Caeiro, P. González, D. Guede, Biomecánica y hueso (y II): ensayos en los distintos niveles jerárquicos del hueso y técnicas alternativas para la determinación de la resistencia ósea, Rev. Osteoporos. y Metab. Miner. 5 (2013) 99–108, https://doi.org/10.4321/S1889-836X2013000200007.

[25] A. Tampieri, M. Iafisco, M. Sandri, S. Panseri, C. Cunha, S. Sprio, E. Savini, M. Uhlarz, T. Herrmannsdörfer, Magnetic bioinspired hybrid nanostructured collagen-hydroxyapatite scaffolds supporting cell proliferation and tuning regenerative process, ACS Appl. Mater. Interfaces. 6 (2014) 15697–15707, https://doi.org/10.1021/am5050967.

[26] E.S. Gadelmawla, M.M. Koura, T.M.A. Maksoud, I.M. Elewa, H.H. Soliman, Roughness parameters, J. Mater. Process. Technol. 123 (2002) 133–145, https://doi.org/10.1016/S0924-0136(02)00060-2.

[27] M.C. Vincent, S. Álvarez, J. Lora, E. Bergantiños, Fouling dynamics modelling in the ultrafiltration of PEGs, Desalination 222 (2008) 451–456, https://doi.org/10.1016/j.desal.0000.00.000.

[28] W.C. Chen, C.H. Chen, H.W. Tseng, Y.W. Liu, Y.P. Chen, C.H. Lee, Y.J. Kuo, C.H. Hsu, Y.M. Sun, Surface functionalized electrospun fibrous poly(3-hydroxybutyrate) membranes and sleeves: a novel approach for fixation in anterior cruciate ligament reconstruction, J. Mater. Chem. B. 5 (2017) 553–564, https://doi.org/10.1039/c6tb02671k.

[29] F. Cuomo, M. Cofelice, F. Lopez, Rheological characterization of hydrogels from alginate-based nanodispersion, Polymers (Basel) 11 (2019), https://doi.org/10.3390/polym11020259.

[30] A.T. Neffe, A. Loebus, A. Zaupa, C. Stoetzel, F.A. Müller, A. Lendlein, Gelatin functionalization with tyrosine derived moieties to increase the interaction with hydroxyapatite fillers, Acta Biomater. 7 (2011) 1693–1701, https://doi.org/10.1016/j.actbio.2010.11.025.

[31] J. Férec, E. Bertevas, B.C. Khoo, G. Ausias, N. Phan-Thien, A rheological constitutive model for semiconcentrated rod suspensions in Bingham fluids, Phys. Fluids 29 (2017), https://doi.org/10.1063/1.4995436.

[32] B.S. Chae, Y.S. Lee, M.S. Jhon, The scaling behavior of a highly aggregated colloidal suspension microstructure and its change in shear flow, Colloid Polym. Sci. 282 (2004) 236–242, https://doi.org/10.1007/s00396-003-0924-z.

[33] D. Bonn, P. Coussot, H.T. Huynh, F. Bertrand, G. Debrégeas, Rheology of soft glassy materials, Europhys. Lett. 59 (2002) 786–792, https://doi.org/10.1209/epl/i2002-00195-4.

[34] L.F. Sukhodub, L.B. Sukhodub, O. Litsis, Y. Prylutskyy, Synthesis and characterization of hydroxyapatite-alginate nanostructured composites for the controlled drug release, Mater. Chem. Phys. 217 (2018) 228–234, https://doi.org/10.1016/j.matchemphys.2018.06.071.

[35] J. Barros, M.P. Ferraz, J. Azeredo, M.H. Fernandes, P.S. Gomes, F.J. Monteiro, Alginate-nanohydroxyapatite hydrogel system: Optimizing the formulation for enhanced bone regeneration, Mater. Sci. Eng. C. 105 (2019), https://doi.org/10.1016/j.msec.2019.109985 109985.

[36] C. Sharma, A.K. Dinda, P.D. Potdar, C.F. Chou, N.C. Mishra, Fabrication and characterization of novel nano-biocomposite scaffold of chitosan-gelatin-alginate-hydroxyapatite for bone tissue engineering, Mater. Sci. Eng. C. 64 (2016) 416–427, https://doi.org/10.1016/j.msec.2016.03.060.

[37] Y. Guesmi, H. Agougui, R. Lafi, M. Jabli, A. Hafiane, Synthesis of hydroxyapatite-sodium alginate via a co-precipitation technique for efficient adsorption of Methylene Blue dye, J. Mol. Liq. 249 (2018) 912–920, https://doi.org/10.1016/j.molliq.2017.11.113.

[38] R. Mishra, B. Basu, A. Kumar, Physical and cytocompatibility properties of bioactive glass-polyvinyl alcohol-sodium alginate biocomposite foams prepared via sol-gel processing for trabecular bone regeneration, J. Mater. Sci. Mater. Med. 20 (2009) 2493–2500, https://doi.org/10.1007/s10856-009-3814-1.

[39] S. Datta, A.P. Rameshbabu, K. Bankoti, P.P. Maity, D. Das, S. Pal, S. Roy, R. Sen, S. Dhara, Oleoyl-chitosan-based nanofiber mats impregnated with amniotic membrane derived stem cells for accelerated full-thickness excisional wound

healing, ACS Biomater. Sci. Eng. 3 (2017) 1738–1749, https://doi.org/10.1021/acsbiomaterials.7b00189.

[40] J.A. Motherway, P. Verschueren, G. Van der Perre, J. Vander Sloten, M.D. Gilchrist, The mechanical properties of cranial bone: the effect of loading rate and cranial sampling position, J. Biomech. 42 (2009) 2129–2135, https://doi.org/10.1016/j.jbiomech.2009.05.030.

[41] J. Hilborn, L.M. Bjursten, A new and evolving paradigm for biocompatibility, J. Tissue Eng. Regen. Med. 1 (2007) 110–119, https://doi.org/10.1002/term.4.

[42] D.L. Kopperdahl, T.M. Keaveny, Yield strain behavior of trabecular bone, J. Biomech. 31 (1998) 601–608, https://doi.org/10.1016/S0021-9290(98)00057-8.

[43] H.H. Bayraktar, E.F. Morgan, G.L. Niebur, G.E. Morris, E.K. Wong, T.M. Keaveny, Comparison of the elastic and yield properties of human femoral trabecular and cortical bone tissue, J. Biomech. 37 (2004) 27–35, https://doi.org/10.1016/S0021-9290(03)00257-4.

[44] D. Huang, L. Niu, J. Li, J. Du, Y. Wei, Y. Hu, X. Lian, W. Chen, K. Wang, Reinforced chitosan membranes by microspheres for guided bone regeneration, J. Mech. Behav. Biomed. Mater. 81 (2018) 195–201, https://doi.org/10.1016/j.jmbbm.2018.03.006.

[45] C.E. Misch, Z. Qu, M.W. Bidez, Mechanical properties of trabecular bone in the human mandible: implications for dental implant treatment planning and surgical placement, J. Oral Maxillofac. Surg. 57 (1999) 700–706, https://doi.org/10.1016/S0278-2391(99)90437-8.

[46] S. Mali, L.S. Sakanaka, F. Yamashita, M.V.E. Grossmann, Water sorption and mechanical properties of cassava starch films and their relation to plasticizing effect, Carbohydr. Polym. 60 (2005) 283–289, https://doi.org/10.1016/j.carbpol.2005.01.003.

[47] C. Xianmiao, L. Yubao, Z. Yi, Z. Li, L. Jidong, W. Huanan, Properties and in vitro biological evaluation of nano-hydroxyapatite/chitosan membranes for bone guided regeneration, Mater. Sci. Eng. C. 29 (2009) 29–35, https://doi.org/10.1016/j.msec.2008.05.008.

[48] S.H. Teng, E.J. Lee, B.H. Yoon, D.S. Shin, H.E. Kim, J.S. Oh, Chitosan/nanohydroxyapatite composite membranes via dynamic filtration for guided bone regeneration, J. Biomed. Mater. Res. - Part A. 88 (2009) 569–580, https://doi.org/10.1002/jbm.a.31897.

[49] J. Mota, N. Yu, S.G. Caridade, G.M. Luz, M.E. Gomes, R.L. Reis, J.A. Jansen, X. Frank Walboomers, J.F. Mano, Chitosan/bioactive glass nanoparticle composite membranes for periodontal regeneration, Acta Biomater. 8 (2012) 4173–4180, https://doi.org/10.1016/j.actbio.2012.06.040.

[50] M. Dziadek, B. Zagrajczuk, E. Menaszek, K. Cholewa-Kowalska, A new insight into in vitro behaviour of poly(ε-caprolactone)/bioactive glass composites in biologically related fluids, J. Mater. Sci. 53 (2018) 3939–3958, https://doi.org/10.1007/s10853-017-1839-2.

[51] D.O. Costa, P.D.H. Prowse, T. Chrones, S.M. Sims, D.W. Hamilton, A.S. Rizkalla, S. J. Dixon, The differential regulation of osteoblast and osteoclast activity by surface topography of hydroxyapatite coatings, Biomaterials 34 (2013) 7215–7226, https://doi.org/10.1016/j.biomaterials.2013.06.014.

[52] Q.L. Loh, C. Choong, Three-dimensional scaffolds for tissue engineering applications: role of porosity and pore size, Tissue Eng. Part B Rev. 19 (2013) 485–502, https://doi.org/10.1089/ten.teb.2012.0437.

[53] M. Masoudi Rad, S. Nouri Khorasani, L. Ghasemi-Mobarakeh, M.P. Prabhakaran, M.R. Foroughi, M. Kharaziha, N. Saadatkish, S. Ramakrishna, Fabrication and characterization of two-layered nanofibrous membrane for guided bone and tissue regeneration application, Mater. Sci. Eng. C. 80 (2017) 75–87, https://doi.org/10.1016/j.msec.2017.05.125.

[54] Q. Wang, R. Hou, Y. Cheng, J. Fu, Super-tough double-network hydrogels reinforced by covalently compositing with silica-nanoparticles, Soft Matter. 8 (2012) 6048, https://doi.org/10.1039/c2sm07233e.

[55] T. Kokubo, H. Takadama, How useful is SBF in predicting in vivo bone bioactivity?, Biomaterials 27 (2006) 2907–2915, https://doi.org/10.1016/j.biomaterials.2006.01.017.

[56] M.S. Laranjeira, M.H. Fernandes, F.J. Monteiro, Innovative macroporous granules of nanostructured-hydroxyapatite agglomerates: Bioactivity and osteoblast-like cell behaviour, J. Biomed. Mater. Res. Part A. 95A (2010) 891–900, https://doi.org/10.1002/jbm.32916.

[57] J.L. Simon, T. Dutta Roy, J.R. Parsons, E.D. Rekow, V.P. Thompson, J. Kemnitzer, J. L. Ricci, Engineered cellular response to scaffold architecture in a rabbit trephine defect, J. Biomed. Mater. Res. - Part A. 66 (2003) 275–282, https://doi.org/10.1002/jbm.a.10569.

[58] V. Karageorgiou, D. Kaplan, Porosity of 3D biomaterial scaffolds and osteogenesis, Biomaterials. 26 (2005) 5474–5491, https://doi.org/10.1016/j.biomaterials.2005.02.002.

[59] K.N. Hansson, S. Hansson, Skewness and Kurtosis: important parameters in the characterization of dental implant surface roughness—a computer simulation, ISRN Mater. Sci. 2011 (2011) 1–6, https://doi.org/10.5402/2011/305312.

[60] N. Tayebi, A.A. Polycarpou, Modeling the effect of skewness and kurtosis on the static friction coefficient of rough surfaces, Tribol. Int. 37 (2004) 491–505, https://doi.org/10.1016/j.triboint.2003.11.010.

[61] S. Hansson, Surface roughness parameters as predictors of anchorage strength in bone: a critical analysis, J. Biomech. 33 (2000) 1297–1303, https://doi.org/10.1016/S0021-9290(00)00045-2.

[62] A.C. Hernández-González, L. Téllez-Jurado, L.M. Rodríguez-Lorenzo, Alginate hydrogels for bone tissue engineering, from injectables to bioprinting: a review, Carbohydr. Polym. 229 (2020), https://doi.org/10.1016/j.carbpol.2019.115514 115514.